Dalton Transactions

ROYAL SOCIETY OF CHEMISTRY

PAPER

View Article Online
View Journal | View Issue

Cite this: *Dalton Trans.*, 2020, **49**, 891

Reduction-induced CO dissociation by a $[Mn(bpy)(CO)_4][SbF_6]$ complex and its relevance in electrocatalytic CO_2 reduction†

Hsin-Ya Kuo, ‡ Steven E. Tignor,‡ Tia S. Lee, Danrui Ni, James Eujin Park, Gregory D. Scholes and Andrew B. Bocarsly *

Received 24th October 2019,
Accepted 11th December 2019

DOI: 10.1039/c9dt04150h

rsc.li/dalton

$[Mn(bpy)(CO)_3Br]$ is recognized as a benchmark electrocatalyst for CO_2 reduction to CO, with the doubly reduced $[Mn(bpy)(CO)_3]^-$ proposed to be the active species in the catalytic mechanism. The reaction of this intermediate with CO_2 and two protons is expected to produce the tetracarbonyl cation, $[Mn(bpy)(CO)_4]^+$, thereby closing the catalytic cycle. However, this species has not been experimentally observed. In this study, $[Mn(bpy)(CO)_4][SbF_6]$ (**1**) was directly synthesized and found to be an efficient electrocatalyst for the reduction of CO_2 to CO in the presence of H_2O. Complex **1** was characterized using X-ray crystallography as well as IR and UV-Vis spectroscopy. The redox activity of **1** was determined using cyclic voltammetry and compared with that of benchmark manganese complexes, *e.g.*, $[Mn(bpy)(CO)_3Br]$ (**2**) and $[Mn(bpy)(CO)_3(MeCN)][PF_6]$ (**3**). Infrared spectroscopic analyses indicated that CO dissociation occurs after a single-electron reduction of complex **1**, producing a $[Mn(bpy)(CO)_3(MeCN)]^+$ species. Complex **1** was experimentally verified as both a precatalyst and an on-cycle intermediate in homogeneous Mn-based electrocatalytic CO_2 reduction.

Introduction

CO_2 reductions are thermodynamically uphill[1] and mechanistically complex, involving multiple proton-coupled electron transfer (PCET) processes,[2] and hence require efficient catalysts.[3] Among the various suitable methods, electrochemical CO_2 reduction utilizing transition metal complexes has attracted much attention[3–10] due to the ease of tunability both at the metal and ligand sites.[11] Moreover, many molecular electrocatalysts are capable of reducing CO_2 to CO, which can be further transformed into hydrocarbons *via* Fischer–Tropsch synthesis.[12]

In molecular CO_2-reduction electrocatalysts, the polypyridine ligand not only stabilizes the reduced metal center but also functions as a redox-active site *via* the conjugated π system, thereby enabling the multiple electron transfer steps necessary for CO_2 transformation.[3] Recently, owing to the high cost and low abundance of second- and third-row transition metals, focus has shifted towards first-row transition metals.[8] For example, the electrocatalytic activity of $[Mn(bpy)(CO)_3Br]$ for CO_2 reduction was first reported by Bourrez *et al.* in 2011.[10] The use of weak Brønsted acids was necessary for this Mn electrocatalyst to be active towards CO_2 reduction.[10,13]

The proposed mechanism, shown in Fig. 1 is favored based on experimental observations[14,15] and theoretical investigations.[16,17]

The active catalyst, $[Mn(bpy)(CO)_3]^-$ (red box, Fig. 1), generated by two one-electron reductions of $[Mn(bpy)(CO)_3Br]$ along with Br^- loss, has an open coordination site. Binding of CO_2 to the open coordination site is followed by protonation to yield $[Mn(bpy)(CO)_3(CO_2H)]$. A final protonation followed by H_2O loss generates $[Mn(bpy)(CO)_4]^+$ (blue box, Fig. 1), which then undergoes a one-electron reduction, CO liberation, and a second electron reduction to regenerate the active catalyst. The tetracarbonyl cation however, has not been experimentally verified as an intermediate in the Mn-based catalytic cycle, although it seems chemically reasonable to suggest its presence.[18] Demonstration of the existence and reaction chemistry of the key $[Mn(bpy)(CO)_4]^+$ intermediate is thus central to confirming the proposed mechanism.

Herein, we present the synthesis and characterization of the tetracarbonyl complex $[Mn(bpy)(CO)_4][SbF_6]$ (**1**). We compare its electrochemical properties with those of two benchmark catalysts, $[Mn(bpy)(CO)_3Br]$ (**2**) and $[Mn(bpy)(CO)_3(MeCN)][PF_6]$ (**3**), and study its role in the mechanism for CO_2 reduction using electrochemistry, FT-IR, and UV-Vis spectroelectrochemistry.

Department of Chemistry, Princeton University, Princeton, New Jersey 08544, USA. E-mail: bocarsly@princeton.edu

†Electronic supplementary information (ESI) available. CCDC 1906434. For ESI and crystallographic data in CIF or other electronic format see DOI: 10.1039/c9dt04150h

‡These authors contributed equally to this work.

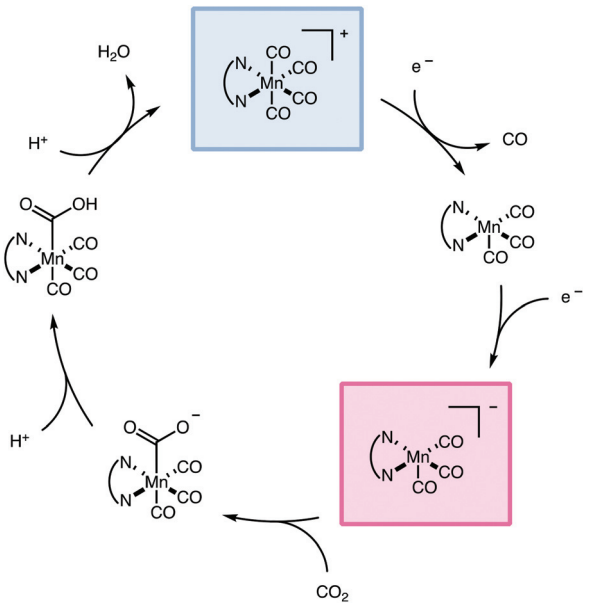

Fig. 1 Proposed mechanism for CO_2 reduction to CO by $[Mn(bpy)(CO)_4]^+$ (blue box) by way of the active species $[Mn(bpy)(CO)_3]^-$ (red box) in the presence of weak Brønsted acids.

Results and discussion

Synthesis and characterization

Based on the reported synthesis of $[Re(bpy)(CO)_4]^+$,[18,19] the preparation of **1** was expected to proceed *via* the metathesis of $Mn(CO)_5Br$ with silver triflate (AgOTf) in CH_2Cl_2 (Scheme 1a), followed by the addition of bpy to produce the desired product. However, this synthetic approach generated an intractable mixture. Unlike the stable $Re(CO)_5(OTf)$,[19] this undesirable result may be attributed to the sensitivity of $Mn(CO)_5(OTf)$ to light and moisture, which caused partial decomposition to yield $Mn_2(CO)_{10}$,[20] making the ligation of bpy impossible.

An alternative approach was carried out by treating **2** with $AgSbF_6$ in CH_2Cl_2 under continuous purging with CO,[21] to yield the desired complex as a SbF_6^- salt. Compared to the condition without added CO, the continuous CO purging significantly inhibited side reactions, and a moderate yield of **1** was obtained (40%) after 30 min. As shown in Scheme 1b, the formation of **1** likely involves the generation of the Lewis acid–base adduct $[Mn(bpy)(CO)_3(SbF_6)]$, followed by CO substitution.[21,22] This intermediate seems to be relatively unstable due to the weakly coordinating SbF_6 anion, and thus it should be noted that the purity of **1** is sensitive to the reaction time. After a prolonged reaction time (4 h), we found byproducts that could not be effectively separated *via* purification. Complex **1** was characterized using UV-Vis, NMR, and FT-IR spectroscopies, as well as X-ray crystallography.

Complexes **1–3** are presented in Fig. 2a, and the UV-Vis absorbance spectrum in MeCN (Fig. 2b) shows a broad peak in the near-UV-visible range corresponding to a metal-to-ligand charge transfer (MLCT) absorption, *i.e.*, Mn(I) → bpy(π*). Consistent with the spectrochemical series, complex **1**, bearing two carbonyl ligands in the axial position, displays the most blue-shifted MLCT band at ~330 nm, whereas complexes **2** and **3**, with axial ligation of bromide and MeCN, exhibit MLCT bands at 416 and 369 nm, respectively. This effect of axial ligand substitution on the MLCT shift is consistent with those of other reported Mn-carbonyl pyridyl-carbene-based complexes.[23] The axial ligands (CO, Br, and MeCN) all exhibit σ-type interaction between the metal d_{z^2} orbital and the ligand orbitals. Furthermore, CO and Br also participate *via* π-type interactions: CO can accept metal electron density into its empty π* orbital through back-bond donation, yielding a large HOMO–LUMO gap, whereas Br can donate electron density to the metal d-orbital, resulting in a small HOMO–LUMO gap. On the other hand, MeCN can bind to the metal center only *via* a σ-type interaction, as it has no symmetry-allowed orbitals for the aforementioned π bonding.

The FT-IR spectra of the three complexes in MeCN are shown in Fig. 2c, and the solid-state ATR-IR spectra are included in Fig. S1.† Both complexes **2** and **3** exhibit a typical three-peak profile between 1900 and 2100 cm^{-1}, which is consistent with the facial arrangement of tricarbonyl metal com-

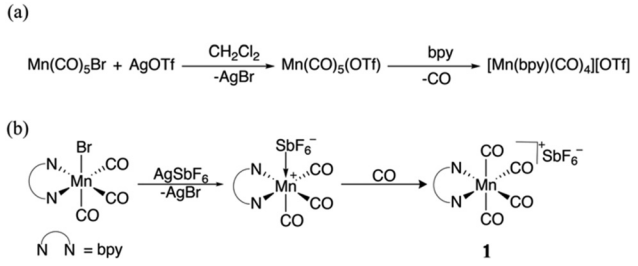

Scheme 1 (a) Proposed synthesis of tetracarbonyl cation *via* $Mn(CO)_5(OTf)$. (b) Formation of **1** *via* Lewis acid–base adduct reaction with CO.

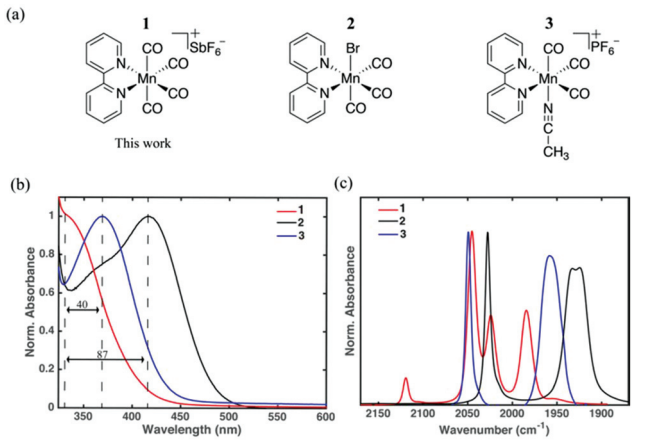

Fig. 2 (a) Representation of the synthesized complexes **1–3**. (b) UV-Vis absorption spectra in MeCN at 298 K at 1 cm path length with MLCT band positions shown. CO- and MeCN-ligated complexes **1** and **3** display a higher-energy MLCT band compared to Br-ligated **2**. (c) Carbonyl stretching bands are evident in the FT-IR spectra.

plexes. The two bands at the lower frequency correspond to symmetric and antisymmetric stretching of the two equatorial COs (*trans* to the bpy), whereas the remaining band at the highest frequency results from the stretching mode of the axial CO,[24,25] which is *trans* to the other axial ligand (*i.e.*, CO, Br, or MeCN). Furthermore, the CO stretching modes of **2** are all at frequencies lower than those of **3**; this shift is consistent with an increase in the π* donation to the carbon of the axial CO in the presence of the π-donor (*i.e.*, Br), and in agreement with the observed MLCT band shift. Complex **1** has C_{2V} symmetry, and is expected to exhibit four IR active carbonyl stretching bands.[26] Analogous to a reported Re complex,[19] these four bands were assigned as an A_1 mode (2130 cm^{-1}), a B_1 mode (2046 cm^{-1}), another A_1 mode (2024 cm^{-1}), and a B_2 mode (1984 cm^{-1}). One striking feature in the IR spectrum of **1** (Fig. 2c) is that one of the A_1 bands appears at an unexpectedly high frequency (2130 cm^{-1}). This indicates a significant decrease in the π-back bond donation between the Mn center and one or more of the CO ligands, and this frequency is near the value for free CO in a heptane solution (2140 cm^{-1}).[21] While it is not surprising that π-back bonding effects were diminished in the *trans*-CO geometry, the shift of one CO stretching frequency so far upfield was unexpected.

We performed density functional theory (DFT) calculations at the M06 level of theory to study the vibrational modes of interest in complex **1**. The vibrational spectrum was computed at the optimized geometry, and the simulated vibrational spectrum is in agreement with the experimental data (Fig. S2†). Four intense CO stretching bands were calculated (unscaled) at 2210, 2119, 2109, and 2072 cm^{-1}. The displacement vectors of the carbonyl vibration modes are included in Fig. S3.† The mode calculated at 2210 cm^{-1} (*i.e.*, the highest CO stretching frequency) shows that all the four CO ligands move in phase (*i.e.*, symmetric stretching) and one of the axial CO ligands exhibits an amplitude slightly different from that of the others. In accord with the experimental data, this suggests that the large shift of the highest stretching frequency (experimentally found to be 2130 cm^{-1}) can be explained by a group stretching vibration of all the four carbonyl ligands. The second-highest stretching frequency at 2119 cm^{-1} is assigned to the two axial COs moving out of phase, *i.e.*, asymmetric stretching. The remaining two modes at 2109 and 2072 cm^{-1} correspond to the symmetric and asymmetric stretching of the two equatorial CO ligands, respectively.

Complex **1** was recrystallized by vapor diffusion of hexane into a concentrated dichloromethane solution. Single crystal X-ray diffraction analysis of the sample yielded the structure shown in Fig. 3; the selected bond lengths and angles are listed in Table 1. The C_{11}–Mn–C_{14} angle (177.01°) is similar to those of reported bpy-ligated Re tetracarbonyl analogs,[18,27] ranging from 177–179°. This bond angle is in agreement with a DFT-calculated value of 177.93° and indicates that the level of theory applied is suitable for describing the current system. An interesting feature of **1** is the significant difference between the two axial CO bond lengths (~0.02 Å), which has also been observed for other Re[18] and Mn[28] tetracarbonyl analogs.

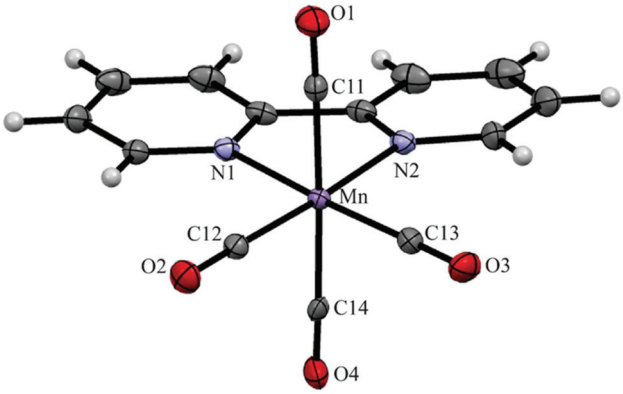

Fig. 3 Molecular structure of **1** with selected atom labelling and thermal ellipsoids shown at 50% probability. Counter anion and solvent are omitted for clarity.

Table 1 Selected bond lengths (Å) and angles (°) for **1**

Mn–C11	1.879(3)
Mn–C12	1.825(3)
Mn–C13	1.837(3)
Mn–C14	1.915(3)
Mn–N1	2.048(3)
Mn–N2	2.044(3)
C11–O1	1.114(5)
C12–O2	1.141(5)
C13–O3	1.135(5)
C14–O4	1.098(5)
N1–Mn–N2	79.0(1)
N1–Mn–C12	95.9(1)
N2–Mn–C13	95.9(1)
C12–Mn–C13	89.2(1)
C11–Mn–C14	177.0(1)

As expected, the two axial Mn–CO bonds show a pronounced difference (1.879 Å *vs.* 1.915 Å); both are longer than the bonds of the two equatorial CO ligands, which are trans to the bpy. This observation is attributed to reduced Mn → CO π-back bonding due to the presence of a strong π acceptor, as evidenced by the FT-IR data. This description is further substantiated by the significantly shorter C_{14}–O_4 bond (1.098 Å).

Electrochemistry

The redox processes of the three complexes under Ar were analyzed using cyclic voltammetry (CV) in MeCN with 0.1 M tetrabutylammonium hexafluorophosphate (TBAH). At a scan rate of 250 mV s^{-1} (Fig. 4a), complex **1** displays two reductive waves at −1.48 and −1.86 V *vs.* Fc/Fc^+; the two reductive peaks do not exhibit return waves over the scan rates ranging from 25 to 1000 mV s^{-1} (Fig. S4†). This lack of reversibility suggests that chemical reactions occur after each reduction, as discussed later. Moreover, a comparison between complex **1** and the reported [Re(bpy)$(CO)_4$][OTf] reveals interesting similarities and differences.[19] The first reduction processes occur at potentials *ca.* 100 mV more positive than those of their neutral pre-

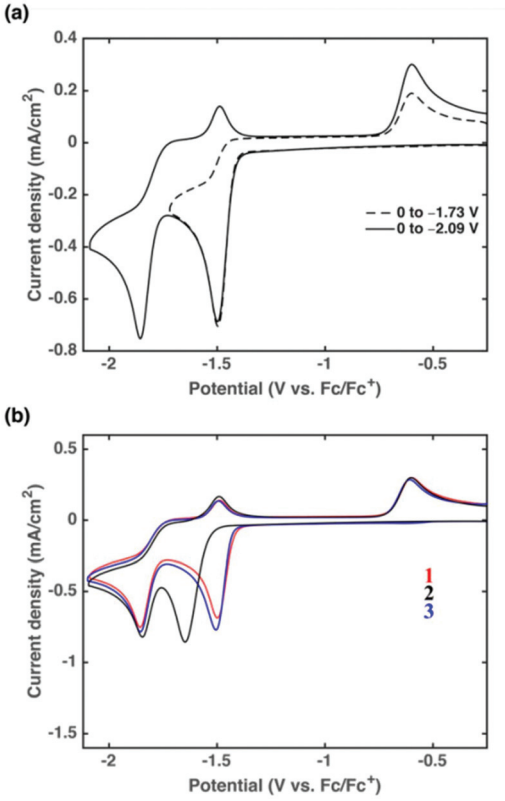

Fig. 4 (a) CV data of **1** (1 mM) at two different switching potentials. The data were recorded at 250 mV s^{-1} under Ar in 0.1 M TBAH in MeCN with a 3 mm-diameter glassy carbon working electrode, a platinum foil counter electrode, and a Ag/Ag^+ nonaqueous reference electrode. All the potentials are referenced to Fc/Fc^+. (b) CV data comparison for the three complexes under study. The other conditions were similar to those shown in panel a.

cursors, *i.e.*, complex **2** or $[Re(bpy)(CO)_3(Cl)]$. However, the first reductive wave of the Re analog remains quasi-reversible, whereas that of **1** is not reversible, which suggests a possible ligand loss.

The CV curve of **1** under Ar is overlaid on those of **2** and **3** in Fig. 4b. The first reduction peaks of **1** and **3** are similar, and they both appear at more positive potentials (~140 mV) than that of **2**. The first reduction seems relatively sensitive to the replacement of the axial bromide with neutral ligands. Furthermore, the lack of reversibility of the first reduction process for these three complexes (*i.e.*, no return wave) suggests a chemical reaction following the first reduction. Analogous to the Re tetracarbonyl species,[18] for which the first reduction is assigned as bpy-based, we propose that the first reduction of **1** is also into the bpy π* orbital, followed by an internal charge transfer to move the electron into a metal centered d-orbital.[29] An electrochemically induced CO dissociation from the singly reduced $[Mn(bpy)(CO)_4]^0$ can be hypothesized to account for this cyclic voltammetric response, which has also been reported for the Re analog. Such reduction-induced CO dissociation was also observed in other systems, including our recently reported CN-bridged Mn complex[30] and other tetracarbonyl analogs containing group 6 metals.[31,32] The subsequent reductions for these three complexes occur at almost identical potentials, and thus suggest similar reductive processes. In line with the literature,[10,13,17,33] Br-ligated **2** readily undergoes Br^- loss followed by dimerization after the first reduction, due to the transient nature of the 16-electron radical $[Mn(bpy)(CO)_3]$ at room temperature.[34] The similar redox processes of complexes **1** and **2** suggest that the second reduction process of **1** is the reduction of $[Mn_2(CO)_6(bpy)_2]$ followed by the formation of $[Mn(bpy)(CO)_3]^-$ *via* dimer cleavage as is discussed in the section on spectroscopic studies.

In the reverse scan, complex **1** shows two oxidative waves at −1.50 and −0.60 V *vs.* Fc/Fc^+; the more cathodic peak only appears after the second reduction potential is reached (Fig. 4a). The two oxidative waves overlap with those of **2** and **3**, as shown in Fig. 4b. The more negative peak is assigned to the oxidation of $[Mn(bpy)(CO)_3]^-$, which leads to dimer formation. The more positive peak is associated with the oxidation of the Mn–Mn-bonded dimer. In addition, in the second reductive scan shown in (Fig. S5†), the first reductive peak of **1** is initiated at a potential slightly more positive than that observed during the first scan; this new potential is consistent with the first reductive onset current of **3**. This observation suggests the possibility of CO dissociation during the first reduction process of **1** and the subsequent formation of the MeCN-coordinated species. The new peak is also apparent in the second scan of **2** (Fig. S5†), which corresponds to the formation of **3** and is in good agreement with the literature.[10]

To gain insight into the species formed upon the one-electron reduction of **1**, we compared the DFT calculations of $[Mn(bpy)(CO)_4]^+$ and $[Mn(bpy)(CO)_4]^0$ at the M06 level of theory. The optimized geometry structure was obtained using the crystal structure of **1** as the initial input. The calculated lowest unoccupied molecular orbital (LUMO) of $[Mn(bpy)(CO)_4]^+$ is localized on the bpy, while the highest occupied molecular orbital (HOMO) is delocalized over the Mn center and the two equatorial COs (Fig. 5a), which is in agreement with the Mn–CO back-bonding evidenced by the experimental data. In comparison, the electronic structure of the singly reduced $[Mn(bpy)(CO)_4]^0$ species reveals differences (Fig. 5b); the LUMO is delocalized over the Mn center and π* orbitals of the two axial CO ligands, whereas the extra electron of the singly occupied molecular orbital resides in the π* orbitals of bpy. Due to orbital overlap, this results in additional electron density on the Mn center and increased π back-bonding into the π* (CO) antibonding orbitals, resulting in a weakening of the CO bonds.[14] In Fig. 5c, the calculated vibration line spectra show that the reduced species $[Mn(bpy)(CO)_4]^0$ exhibits red shifted ν(CO) frequencies relative to the nonreduced counterpart. However, one of the axial CO ligands exhibits relatively decreased π back-bonding. These results suggest the weakening of the metal carbonyl bond interaction in $[Mn(bpy)(CO)_4]^0$, thereby leading to the CO dissociation following one-electron reduction of the initial cationic complex.

To investigate the activity of **1** in the presence of CO_2 with and without water, we studied the electrochemistry of **1** under

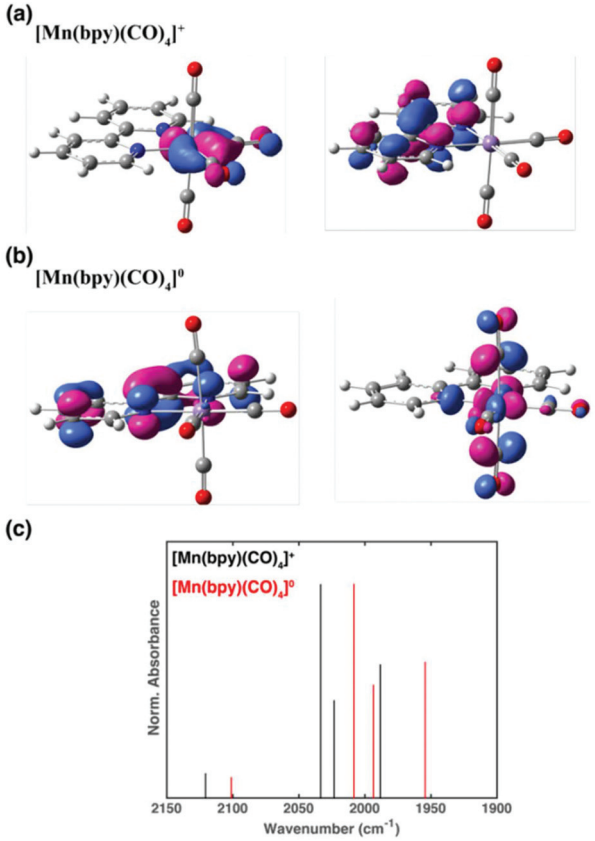

Fig. 5 (a) HOMO (left) and LUMO (right) of $[Mn(bpy)(CO)_4]^+$. (b) SOMO (left) and LUMO (right) of $[Mn(bpy)(CO)_4]^0$. (c) Calculated carbonyl stretching frequencies.

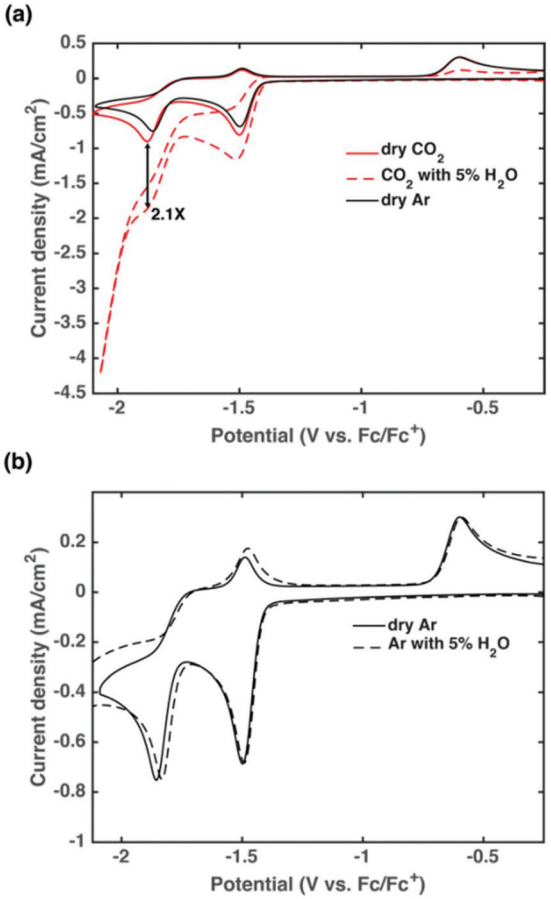

Fig. 6 CV data of **1** with and without 5% H_2O under CO_2 (a) and Ar (b) at 250 mV s^{-1}. All the other conditions were similar to those given in Fig. 4.

dry and wet CO_2, as shown in Fig. 6a. Under dry CO_2 conditions (red solid line), slight current increases were observed at both reduction potentials. Upon addition of H_2O (5%, red dashed line), a significant current enhancement (2.1 times) occurs at the second reduction potential, and the oxidative waves at −1.50 and −0.60 V *vs.* Fc/Fc^+ are diminished; both phenomena indicate that CO_2 reduction is catalyzed by the species associated with the second reduction potential of **1**. Additionally, upon addition of water under CO_2, the shape of the first reduction wave changes with a slight current increase, whereas no significant change occurs for the wet electrolyte under Ar, as shown in Fig. 6b. The effect of the H_2O content on the catalytic activity was surveyed by monitoring the current at −1.88 V *vs.* Fc/Fc^+ (Fig. S6†). Increasing the H_2O amount from 5% to 7% (v/v) did not result in a higher current at the second reduction peak, indicating that at 5% water, the proton demand was saturated.[35] Thus, complex **1** was experimentally demonstrated to be electrochemically active in the presence of CO_2 and H_2O.

To probe this electrochemical reaction, a bulk electrolysis with 25 μmol complex **1** (1 mM) was carried out at −1.88 V *vs.* Fc/Fc^+ in the wet electrolyte under CO_2. Carbon monoxide was identified as the reaction product, and was monitored and quantified through headspace analysis using gas chromatography (GC). The product analysis in Fig. S7a† shows that the amount of CO is directly proportional to the charge passed, with an average faradaic efficiency (ϕ_{CO}) of 80 ± 4.0% for CO production over a 3 h observation period. The remaining charge was balanced H_2 production directly from the electrode surface. No soluble organic products, including formate, were found using ^1H NMR of the post-electrolysis electrolyte (Fig. S8†). This result not only verifies the electrochemical activity of **1** under CO_2 but also suggests that complex **1** is highly selective for CO production. Furthermore, CO was also observed when a bulk electrolysis with **1** (1 mM) was conducted at −1.48 V *vs.* Fc/Fc^+ (the first-reduction peak potential) under otherwise identical conditions. The CO evolution data for both potentials are compared in Fig. S7b.† We noted that the CO evolution at the first reduction potential (−1.48 V *vs.* Fc/Fc^+) reached a plateau after ~2 h; this observation can be attributed to the saturation of coordination sites by MeCN as a result of a single-electron reduction followed by CO dissociation, which is further supported by the formation of **3** (0.9 mM), as evidenced by the post-electrolysis UV-Vis spectrum (Fig. S9†). Upon dividing the moles of CO produced by the moles of **1** (25 μmol) for the three points located in the

plateau regime, a mean value of 0.98 ± 0.05 was obtained, which approximates to unity. These findings indicate that after a single-electron reduction, complex **1** effectively generates vacant sites followed by MeCN coordination.

To further confirm electrocatalysis, we electrolyzed complex **1** (1 mM) at the second reduction peak (−1.88 V *vs.* Fc/Fc^+) in the presence of $^{13}CO_2$ in wet electrolyte. After a 3 h bulk electrolysis, the cell headspace was examined using IR spectroscopy. The gaseous sample contained both ^{13}CO and ^{12}CO, as shown in Fig. 7a. The presence of ^{13}CO confirmed the electrocatalytic conversion of CO_2 to CO. Based on the proposed mechanism (Fig. 1), the presence of ^{12}CO was anticipated; the mechanism involves the formation of an Mn–CO_2H moiety, and subsequent protonation followed by H_2O loss to generate $[Mn(bpy)(CO)_4]^+$. In agreement with that of reported Mn-based electrocatalysts,[35,36] the mechanism under $^{13}CO_2$ results in a $[Mn(bpy)(^{13}CO)(^{12}CO)_3]^+$ intermediate, which subsequently leads to either ^{12}CO or ^{13}CO dissociation before regenerating the active catalyst. Therefore, one can reasonably anticipate as much as a 1 : 3 ratio of ^{13}CO and ^{12}CO in the product stream formed with **1** as a precatalyst and an on-cycle intermediate for electrocatalytic CO_2 reduction to CO (Fig. 7b).

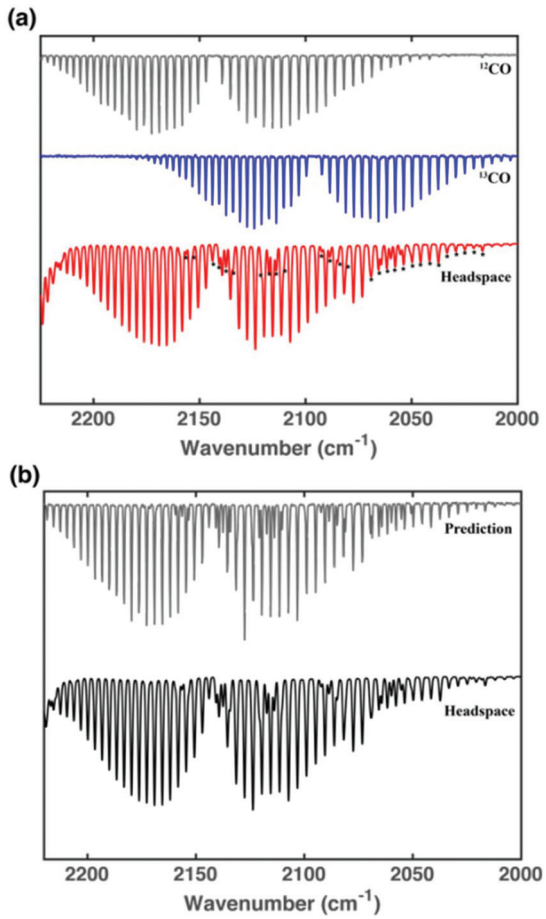

Fig. 7 (a) Analysis of the headspace with FT-IR following a 3 h electrolysis of **1** with $^{13}CO_2$ at −1.86 V *vs.* Fc/Fc^+ in 0.1 M TBAH in MeCN with 5% H_2O. The presence of ^{13}CO (*) confirms the electrocatalytic CO_2 conversion to CO. (b) A plot of the headspace (black trace) is compared with a predicted spectrum with 30% ^{13}CO and 70% ^{12}CO (grey trace).

Table 2 Efficiency comparison of complexes **1** and **2** for the reduction of CO_2 to CO

Complex	ϕ_{CO} [a] (%)	E_{appl} [b] (V)	η [c] (V)	i_{cat}/i_p
1	80	−1.88	0.67	2.1
2	75	−1.86	0.65	1.6

[a] Average ϕ_{CO} obtained from a 3 h bulk electrolysis. [b] Referenced to Fc/Fc^+. [c] Each overpotential was calculated from the difference between the thermodynamic redox potential and the applied potential. The formal redox potential for CO formation is −1.21 V *vs.* Fc/Fc^+ in non-aqueous media.[37]

After electrolyzing 25 μmol of **1** at the second reduction potential under CO_2 for 3 h, we detected 85 μmol of CO (Fig. S7b,† black dots). Considering the CO evolution from the dissociation process in the same time period (Fig. S7b,† blue dots), ~65 μmol of CO can be associated with the catalytic conversion, yielding a turnover number of 2.4. Figures of merit were selected to compare the efficiency of **1** with that of the benchmark catalyst 2, as shown in Table 2. The quantity (i_{cat}/i_p) obtained from CV also provides insight into the relative turnover frequencies.[35] Here, i_{cat} is the peak current under 5% H_2O in MeCN saturated with CO_2, and i_p is the peak current under inert conditions (dry electrolyte). The ratio of i_{cat} to i_p gives information related to the kinetics of the corresponding reaction.

Complex **1** shows a i_{cat}/i_p value that is slightly larger than that of complex **2**; we suspect that this is a result of the increased lability of the axial CO ligand in complex **1** as compared to the lability of the axial Br in complex **2**.

Identification of intermediates pertinent to CO_2 reduction

We studied the first reductive process of **1** using IR spectroscopy. Due to the air sensitivity of the reduced species, bulk electrolysis with **1** was carried out at −1.48 V *vs.* Fc/Fc^+ under a nitrogen atmosphere to avoid any oxygen exposure, and the electrolyte was then transferred into a sealed transmission cell and monitored using FT-IR spectroscopy. After a 5 min bulk electrolysis, the CO bands of the pristine complex disappear and new bands corresponding to complex **3** appear, including a broad band around 1960 cm^{-1} and a sharp band centered at 2050 cm^{-1} (Fig. 8a, grey squares). This new vibrational pattern indicating the presence of a tricarbonyl species further supports the occurrence of CO dissociation at the first reduction potential. The other new bands at 1850–1900 cm^{-1} (with two shoulders at 1930–1970 cm^{-1}) is assigned to the formation of $[Mn_2(CO)_6(bpy)_2]$ (Fig. 8a, black circles). Based on these observations, an EC mechanism is proposed, as shown in Fig. 8b.

However, we did not detect the presence of the singly reduced $[Mn(bpy)(CO)_4]^0$, which is anticipated to be too unstable at room temperature to observe; a similar observation was also reported for the analogous Re system. As discussed in the previous section, $[Mn(bpy)(CO)_4]^0$ can undergo CO dissociation to form the five-coordinate radical $[Mn(bpy)(CO)_3]^0$,

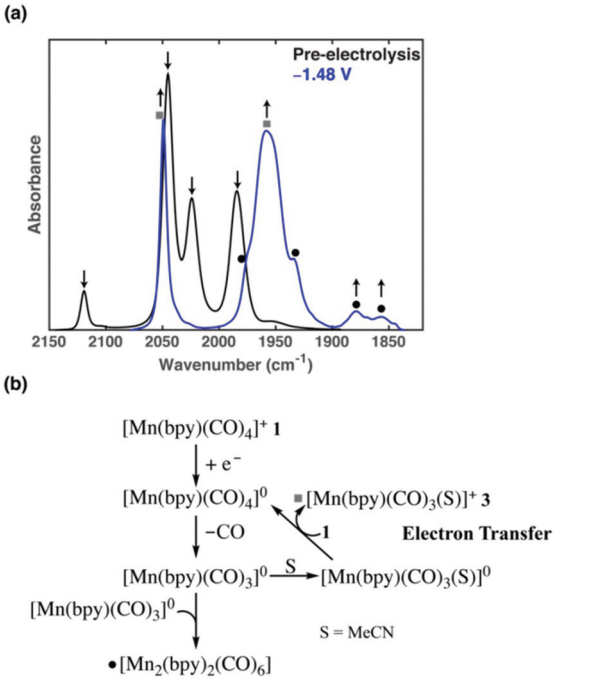

Fig. 8 (a) IR spectral changes of 1 before and after a 5 minutes bulk electrolysis at −1.48 V *vs.* Fc/Fc$^+$ under Ar. The new peaks correspond to the formation of two species: complex **3** (■) and the Mn–Mn bonded dimer (●). (b) Schematic electrochemical reaction mechanism of **1** at the first reduction potential.

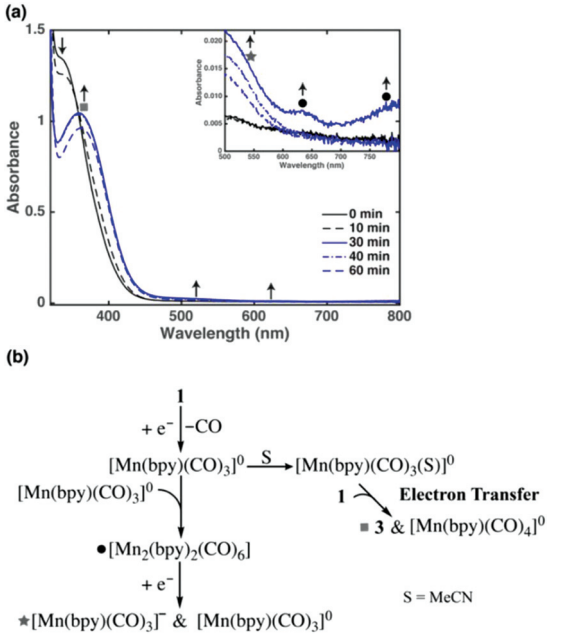

Fig. 9 (a) *In situ* UV-Vis spectral changes for complex **1** at −1.88 V *vs.* Fc/Fc$^+$ under Ar. The new peaks correspond to the formation of the following species: complex **3**, [Mn(bpy)(CO)$_3$]$^-$, and the Mn–Mn-bonded dimer. (b) Schematic mechanism for the formation of [Mn(bpy)(CO)$_3$]$^-$ *via* **1** at the second reduction potential.

which is short-lived at room temperature. This radical can either dimerize or be captured by MeCN to form the solvato radical ([Mn(bpy)(CO)$_3$(MeCN)]^0), which is unstable at room temperature. This solvato intermediate can transfer its electron to **1** to form **3** and [Mn(bpy)(CO)$_4$]^0; the electron transfer is thermodynamically feasible since the reduction potential of **3** is slightly more negative with respect to that of **1** (Fig. 4b). Clearly, the observations of **3** and the Mn–Mn-bonded dimer provide evidence of reduction-induced CO dissociation.

Next, the second reductive process of **1** was monitored *via in situ* UV-Vis spectroscopy, and the results are shown in Fig. 9. During a bulk electrolysis at −1.88 V *vs.* Fc/Fc$^+$ (conducted in a customized quartz cuvette with a Pt gauze working electrode), the band corresponding to **1** (~330 nm) decreased, with a new band growing at ~370 nm and new features at 500–800 nm (Fig. 9a, inset). The former band is attributed to the formation of **3** (grey squares), whereas the new band at ~550 nm reveals the formation of the five-coordinate [Mn(bpy)(CO)$_3$]$^-$ (grey stars). This observation is consistent with the UV-Vis spectral changes of **2** at the second reduction potential (Fig. S11†). Interestingly, both **3** and the Mn–Mn-bonded dimer (black circles) were observed during the second reductive process. In light of the proposed EC mechanism (Fig. 9b), the five-coordinate radical [Mn(bpy)(CO)$_3$]^0 can be involved in several possible pathways in the subsequent reduction (Fig. 9b); it can rapidly dimerize owing to its transient nature, and after receiving the second electron, the dimer can undergo cleavage of the Mn–Mn bond, generating the key intermediate [Mn(bpy)(CO)$_3$]$^-$ and [Mn(bpy)(CO)$_3$]^0. Another possibility is that [Mn(bpy)(CO)$_3$]^0 can be solvated by MeCN to form the solvato radical. This solvato radical can reduce **1** to yield **3** and [Mn(bpy)(CO)$_4$]^0 (as discussed in the previous section). In agreement with the calculation studies, the overall experimental results show that **1** functions as one of the intermediates and as a precatalyst in the Mn-based CO_2 catalytic cycle, as it can generate the five-coordinate anion, [Mn(bpy)(CO)$_3$]$^-$, a critical intermediate to bind and reduce CO_2.

Conclusions

We experimentally demonstrated that the tetracarbonyl cation **1** is a precatalyst and an on-cycle intermediate that can be electrochemically transformed into the active catalyst [Mn(bpy)(CO)$_3$]$^-$ for CO_2 reduction to CO in the presence of a proton source. Complex **1** has been studied using X-ray crystallography, IR and UV-Vis spectroscopy, and DFT calculations. One of the axial Mn–CO bonds exhibits a surprisingly decreased level of π back-bonding. The electrochemical properties of **1** were studied using cyclic voltammetry and compared with those of two benchmark complexes **2** and **3**. Complex **1** undergoes a reduction-induced CO dissociation and subsequent solvation in MeCN. Importantly, the formation of the active catalyst [Mn(bpy)(CO)$_3$]$^-$ *via* two single-electron reductions of **1**, detected using an *in situ* UV-Vis study, indicates that complex **1** is an intermediate present in the Mn-mediated CO_2 electrocatalytic system.

Experimental section

General procedures

All experiments were performed in the absence of light except during the weighing of solid samples. Schlenk techniques and anhydrous solvents were used for the synthesis of all complexes. All reagents (reagent grade) were obtained from commercial suppliers and used without further purification unless otherwise noted. Anhydrous MeCN and CH_2Cl_2 were purchased from Sigma-Aldrich (Sure/Seal). TBAH (Sigma-Aldrich) was dried under vacuum overnight prior to use. Manganese pentacarbonyl bromide (Strem), 2,2′-bipyridine (Sigma-Aldrich), and silver hexafluoroantimonate (Sigma-Aldrich) were used as received. Manganese complexes were carefully handled with minimal light exposure.

Electrochemical studies

For all electrochemical experiments, the electrolyte was bubbled with the desired gas (Ar or CO_2) for 15 min prior to taking a background scan to ensure a featureless background from 0 to −2.9 V *vs.* Fc/Fc^+. After adding the desired complex, the electrolyte was bubbled for an additional 5 min prior to data collection. Complexes were loaded at a concentration of 1 mM for both CV and bulk electrolysis. Ferrocene was added as an internal reference. The total volume of electrolyte used for these experiments was 10 mL for CV and 25 mL for bulk electrolysis. The bulk electrolyses were operated for ∼4 h, and the headspace was analyzed using GC approximately every 20 min. The proton concentration was kept consistent for the Ar and CO_2 trials using pH-adjusted water with $HClO_4$ and neutral water, respectively. Electrolytes were prepared by dissolving TBAH in anhydrous MeCN in a Schlenk flask. The electrolyte was stored under an inert atmosphere and purged immediately prior to use. A 3 mm-diameter glassy carbon disk electrode (BASi MF-2012) was used in all electrochemical experiments. Potentials were first referred to an $Ag/AgNO_3$ (10 mM) electrode (BASi MW-1085) in 0.1 M TBAH/MeCN and then referenced to Fc/Fc^+. A platinum mesh (∼1 cm^2) attached to a platinum wire was used as the counter electrode in all electrochemical measurements. A 15 mL three-neck round-bottom flask was used as the electrochemical cell for CV, and a 70 mL four-neck homemade jacketed flask was used for bulk electrolysis. The working electrode and reference electrodes were secured using "mini" Ace-threaded adaptors from Aceglass (No. 7 and No. 8, respectively). The counter electrode was threaded through a septum, which was then fitted on to one neck of the cell.

Instrumentation

Electrochemical measurements were performed on a Model CHI 760D electrochemical workstation (CH Instruments, Austin, TX). NMR spectra were recorded on a Bruker AVANCE spectrometer (500 MHz for ^1H nuclei and 125 MHz for ^{13}C nuclei). FT-IR spectra were recorded on a Nicolet Model iS50 FT-IR spectrometer for gas and liquid samples, and a Nicolet Model 6700 FT-IR spectrometer equipped with a single-reflection diamond ATR attachment for solid samples. UV-Vis spectra and photoprocesses were monitored using a Cary 60 UV-Vis spectrophotometer (Agilent Technologies). X-ray diffraction data were collected with a Bruker Photon 100 CMOS system equipped with a Mo Kα IμS microfocus source (λ = 0.71073 Å). The frames were integrated with the Bruker SAINT software package using a narrow-frame algorithm. CO production was analyzed using a 70 °C isothermal method over 5 min on an HP 6890 gas chromatograph and TCD with a Molsieve 5A PLOT capillary column (Agilent) running He as the flow gas. H_2 was sampled with an SRI 8610C gas chromatograph and TCD with a Molsieve column (HAYESEP D) and Ar flow gas. A 7 min isotherm at 80 °C was employed.

Computational methodology

Gaussian 16 *via* density functional theory (DFT) with the M06 functional level of theory and 6-311G** basis set were used to perform geometry optimization and frequency calculations of the ground state, singlet and doublet of the molecules of interest. To alleviate computational costs, we applied LANL2D basis set on the manganese metal center. The LANL2D basis set describes the inner electrons of the metal with effective core potentials. Additionally, a solvent continuum model with acetonitrile was utilized, since all electrochemical measurements were conducted in the presence of acetonitrile. All frequency calculations carried out on stationary points yielded zero imaginary frequencies. HOMO and LUMO energy levels were extracted from the calculations.

Syntheses

$[Mn(bpy)(CO)_4][SbF_6]$ (1). $[Mn(bpy)(CO)_3Br]$ (0.15 g, 0.40 mmol) and $AgSbF_6$ (0.21 g, 0.61 mmol) were mixed in 25 mL of anhydrous CH_2Cl_2. CO gas was bubbled through the solution in the absence of light with constant stirring at room temperature. After 40 min, the solution was filtered through a Celite pad and the filtrate was evaporated to yield a yellow solid. Reprecipitation from CH_2Cl_2/Et_2O (1/10, 120 mL) afforded 0.070 g (40% yield) of a yellow microcrystalline solid, which was washed several times with Et_2O and dried *in vacuo*. IR (ATR-IR, ν_{CO} in cm^{-1}): 2116 (s), 2022 (w), 1967 (w), 1938 (sh). UV-Vis data in CH_2Cl_2 (λ_{max} in nm): 330. ^1H NMR (500 MHz, CD_2Cl_2) δ 8.93 (d, J = 5.5 Hz, 1H), 8.44 (d, J = 8.1 Hz, 1H), 8.31 (t, J = 7.9 Hz, 1H), 7.78 (t, J = 6.6 Hz, 1H). ^{13}C NMR (126 MHz, CD_2Cl_2) δ 213.55, 205.02, 156.00, 154.92, 141.71, 129.08, 124.90.

$[Mn(bpy)(CO)_3Br]$ (2). This complex was synthesized according to the literature[5] and characterized using IR spectroscopy in MeCN (ν_{CO} in cm^{-1}): 2028 (s), 1930 (m).

$[Mn(bpy)(CO)_3(MeCN)][PF_6]$ (3). This complex was also synthesized according to the literature.[5] IR spectroscopy in MeCN (ν_{CO} in cm^{-1}): 2050 (s), 1958 (w). ^1H NMR (500 MHz, CD_3CN) δ 9.14 (d, J = 5.5 Hz, 1H), 8.40 (d, J = 8.1 Hz, 1H), 8.23 (td, J = 7.9, 1.5 Hz, 1H), 7.71 (dd, J = 7.6, 5.6 Hz, 1H). ^{13}C NMR (126 MHz, CD_3CN) δ 218.95, 217.97, 156.50, 154.96, 140.85, 128.14, 127.90, 124.14.

Conflicts of interest

There are no conflicts to declare.

Acknowledgements

Financial support for this work was provided by the National Science Foundation under grant CHE-1800400. Any opinions, findings, and conclusions or recommendations expressed in this material are those of the authors and do not necessarily reflect the views of the National Science Foundation.

Notes and references

1 J. L. White, M. F. Baruch, J. E. Pander, Y. Hu, I. C. Fortmeyer, J. E. Park, T. Zhang, K. Liao, J. Gu, Y. Yan, *et al.* Light-Driven Heterogeneous Reduction of Carbon Dioxide: Photocatalysts and Photoelectrodes, *Chem. Rev.*, 2015, **115**(23), 12888–12935.

2 D. C. Grills, M. Z. Ertem, M. McKinnon, K. T. Ngo and J. Rochford, Mechanistic Aspects of CO_2 Reduction Catalysis with Manganese-Based Molecular Catalysts, *Coord. Chem. Rev.*, 2018, **374**, 173–217.

3 N. Elgrishi, M. B. Chambers, X. Wang and M. Fontecave, Molecular Polypyridine-Based Metal Complexes as Catalysts for the Reduction of CO_2, *Chem. Soc. Rev.*, 2017, **46**(3), 761–796.

4 K. A. Grice, Carbon Dioxide Reduction with Homogenous Early Transition Metal Complexes: Opportunities and Challenges for Developing CO_2 Catalysis, *Coord. Chem. Rev.*, 2017, **336**, 78–95.

5 C. Costentin, M. Robert and J.-M. Savéant, Catalysis of the Electrochemical Reduction of Carbon Dioxide, *Chem. Soc. Rev.*, 2013, **42**(6), 2423–2436, DOI: 10.1039/C2CS35360A.

6 M. Stanbury, J.-D. Compain and S. Chardon-Noblat, Electro and Photoreduction of CO_2 Driven by Manganese-Carbonyl Molecular Catalysts, *Coord. Chem. Rev.*, 2018, **361**, 120–137.

7 J. Hawecker, J.-M. Lehn and R. Ziessel, Electrocatalytic Reduction of Carbon Dioxide Mediated by $Re(Bipy)(CO)_3Cl$ (Bipy = 2,2′-Bipyridine), *J. Chem. Soc., Chem. Commun.*, 1984, (6), 328–330.

8 H. Takeda, C. Cometto, O. Ishitani and M. Robert, Electrons, Photons, Protons and Earth-Abundant Metal Complexes for Molecular Catalysis of CO_2 Reduction, *ACS Catal.*, 2017, **7**(1), 70–88.

9 A. Sinopoli, N. T. La Porte, J. F. Martinez, M. R. Wasielewski and M. Sohail, Manganese Carbonyl Complexes for CO_2 Reduction, *Coord. Chem. Rev.*, 2018, **365**, 60–74.

10 M. Bourrez, F. Molton, S. Chardon-Noblat and A. Deronzier, $[Mn(Bipyridyl)(CO)_3Br]$: An Abundant Metal Carbonyl Complex as Efficient Electrocatalyst for CO_2 Reduction, *Angew. Chem., Int. Ed.*, 2011, **50**(42), 9903–9906.

11 R. Francke, B. Schille and M. Roemelt, Homogeneously Catalyzed Electroreduction of Carbon Dioxide—Methods, Mechanisms, and Catalysts, *Chem. Rev.*, 2018, **118**(9), 4631–4701.

12 C. Graves, S. D. Ebbesen, M. Mogensen and K. S. Lackner, Sustainable Hydrocarbon Fuels by Recycling CO_2 and H_2O with Renewable or Nuclear Energy, *Renewable Sustainable Energy Rev.*, 2011, **15**(1), 1–23.

13 J. M. Smieja, M. D. Sampson, K. A. Grice, E. E. Benson, J. D. Froehlich and C. P. Kubiak, Manganese as a Substitute for Rhenium in CO_2 Reduction Catalysts: The Importance of Acids, *Inorg. Chem.*, 2013, **52**(5), 2484–2491.

14 D. C. Grills, J. A. Farrington, B. H. Layne, S. V. Lymar, B. A. Mello, J. M. Preses and J. F. Wishart, Mechanism of the Formation of a Mn-Based CO_2 Reduction Catalyst Revealed by Pulse Radiolysis with Time-Resolved Infrared Detection, *J. Am. Chem. Soc.*, 2014, **136**(15), 5563–5566.

15 M. Bourrez, M. Orio, F. Molton, H. Vezin, C. Duboc, A. Deronzier and S. Chardon-Noblat, Pulsed-EPR Evidence of a Manganese(II) Hydroxycarbonyl Intermediate in the Electrocatalytic Reduction of Carbon Dioxide by a Manganese Bipyridyl Derivative, *Angew. Chem., Int. Ed.*, 2014, **53**(1), 240–243.

16 C. Riplinger and E. A. Carter, Influence of Weak Brønsted Acids on Electrocatalytic CO_2 Reduction by Manganese and Rhenium Bipyridine Catalysts, *ACS Catal.*, 2015, **5**(2), 900–908.

17 C. Riplinger, M. D. Sampson, A. M. Ritzmann, C. P. Kubiak and E. A. Carter, Mechanistic Contrasts between Manganese and Rhenium Bipyridine Electrocatalysts for the Reduction of Carbon Dioxide, *J. Am. Chem. Soc.*, 2014, **136**(46), 16285–16298.

18 K. A. Grice, N. X. Gu, M. D. Sampson and C. P. Kubiak, Carbon Monoxide Release Catalysed by Electron Transfer: Electrochemical and Spectroscopic Investigations of $[Re(Bpy\text{-}R)(CO)_4](OTf)$ Complexes Relevant to CO_2 Reduction, *Dalton Trans.*, 2013, **42**(23), 8498–8503.

19 R. J. Shaver and D. P. Rillema, Physical and Photophysical Properties of Rhenium(I) Tetracarbonyl Complexes, *Inorg. Chem.*, 1992, **31**(20), 4101–4107.

20 S. P. Schmidt, J. Nitschke, W. C. Trogler, S. I. Huckett and R. J. Angelici, in *Inorganic Syntheses*, John Wiley & Sons, Ltd, 2007, pp. 113–117.

21 V. Yempally, S. J. Kyran, R. K. Raju, W. Y. Fan, E. N. Brothers, D. J. Darensbourg and A. A. Bengali, Thermal and Photochemical Reactivity of Manganese Tricarbonyl and Tetracarbonyl Complexes with a Bulky Diazabutadiene Ligand, *Inorg. Chem.*, 2014, **53**(8), 4081–4088.

22 W. Beck and K. Suenkel, Metal Complexes of Weakly Coordinating Anions. Precursors of Strong Cationic Organometallic Lewis Acids, *Chem. Rev.*, 1988, **88**(7), 1405–1421.

23 J. Agarwal, C. J. S. Iii, T. W. Shaw, J. E. Vandezande, G. F. Majetich, A. B. Bocarsly and H. F. S. Iii, Exploring the Effect of Axial Ligand Substitution (X = Br, NCS, CN) on the

Photodecomposition and Electrochemical Activity of [MnX(N–C)(CO)$_3$] Complexes, *Dalton Trans.*, 2015, **44**(5), 2122–2131.

24 C. Pereira, H. G. Ferreira, M. S. Schultz, J. Milanez, M. Izidoro, P. C. Leme, R. H. A. Santos, M. T. P. Gambardella, E. E. Castellano, B. S. Lima-Neto, *et al.* Probing the Electronic Factors Responsible for the Cyclic Electron-Transfer Induced Isomerism Fac⇄mer: Synthesis, Electrochemical and Spectroscopic Studies of Fac-[Mn(CO)$_3$(L′–L′)L]$^{0/+}$ Complexes, *Inorg. Chim. Acta*, 2005, **358**(13), 3735–3744.

25 B. S. Ault, T. M. Becker, G. Q. Li and M. Orchin, The Infrared Spectra and Theoretical Calculations of Frequencies of Fac-Tricarbonyl Octahedral Complexes of Manganese(I), *Spectrochim. Acta, Part A*, 2004, **60**(11), 2567–2572.

26 B. Hutchinson and K. Nakamoto, Infrared Spectra of Group VIB Metal Carbonyls Containing Heterocyclic Diamines, *Inorg. Chim. Acta*, 1969, **3**, 591–595.

27 T. Scheiring, W. Kaim and J. Fiedler, Geometrical and Electronic Structures of the Acetyl Complex Re(Bpy)(CO)$_3$(COCH$_3$) and of [M(Bpy)(CO)$_4$](OTf), M=Mn,Re, *J. Organomet. Chem.*, 2000, **598**(1), 136–141.

28 G. A. Carriedo, J. A. Pérez-Martínez, D. Miguel, V. Riera, S. García-Granda and E. Pérez-Carreño, The Reduction and Oxidation of Cationic Carbonyl Complexes of Manganese with Phosphoniodithioformate: X-Ray Crystal Structure of [Mn(CO)$_4$(S$_2$CPCy$_3$)]ClO$_4$, *J. Organomet. Chem.*, 1996, **511**(1), 77–84.

29 S. E. Tignor, H.-Y. Kuo, T. S. Lee, G. D. Scholes and A. B. Bocarsly, Manganese-Based Catalysts with Varying Ligand Substituents for the Electrochemical Reduction of CO_2 to CO, *Organometallics*, 2019, **38**(6), 1292–1299.

30 H.-Y. Kuo, T. S. Lee, A. T. Chu, S. E. Tignor, G. D. Scholes and A. B. Bocarsly, A Cyanide-Bridged Di-Manganese Carbonyl Complex That Photochemically Reduces CO_2 to CO, *Dalton Trans.*, 2019, **48**(4), 1226–1236.

31 M. L. Clark, K. A. Grice, C. E. Moore, A. L. Rheingold and C. P. Kubiak, Electrocatalytic CO_2 Reduction by M(Bpy-R)(CO)$_4$ (M = Mo, W; R = H, TBu) Complexes. Electrochemical, Spectroscopic, and Computational Studies and Comparison with Group 7 Catalysts, *Chem. Sci.*, 2014, **5**(5), 1894–1900.

32 J. Tory, B. Setterfield-Price, R. A. W. Dryfe and F. Hartl, [M(CO)$_4$(2,2′-Bipyridine)] (M=Cr, Mo, W) Complexes as Efficient Catalysts for Electrochemical Reduction of CO_2 at a Gold Electrode, *ChemElectroChem*, 2015, **2**(2), 213–217.

33 C. W. Machan, M. D. Sampson, S. A. Chabolla, T. Dang and C. P. Kubiak, Developing a Mechanistic Understanding of Molecular Electrocatalysts for CO_2 Reduction Using Infrared Spectroelectrochemistry, *Organometallics*, 2014, **33**(18), 4550–4559.

34 F. Hartl, B. D. Rossenaar, G. J. Stor and D. J. Stufkens, Role of an Electron-Transfer Chain Reaction in the Unusual Photochemical Formation of Five-Coordinated Anions [Mn(CO)$_3$(α-Diimine)]$^-$ from Fac-[Mn(x)(CO)$_3$(α-Diimine)] (X = Halide) at Low Temperatures, *Recl. Trav. Chim. Pays-Bas*, 1995, **114**(11–12), 565–570.

35 J. Agarwal, T. W. Shaw, H. F. Schaefer and A. B. Bocarsly, Design of a Catalytic Active Site for Electrochemical CO_2 Reduction with Mn(I)-Tricarbonyl Species, *Inorg. Chem.*, 2015, **54**(11), 5285–5294.

36 J. Agarwal, T. W. Shaw, C. J. Stanton, G. F. Majetich, A. B. Bocarsly and H. F. Schaefer, NHC-Containing Manganese(I) Electrocatalysts for the Two-Electron Reduction of CO_2, *Angew. Chem., Int. Ed.*, 2014, **53**(20), 5152–5155.

37 C. Costentin, S. Drouet, M. Robert and J.-M. Savéant, A Local Proton Source Enhances CO_2 Electroreduction to CO by a Molecular Fe Catalyst, *Science*, 2012, **338**(6103), 90–94.